A *SPITZER* IRAC SEARCH FOR SUBSTELLAR COMPANIONS OF THE DEBRIS DISK STAR ε ERIDANI

M. Marengo, S. T. Megeath,[1] and G. G. Fazio
Harvard-Smithsonian Center for Astrophysics, 60 Garden Street, Cambridge, MA 02138; mmarengo@cfa.harvard.edu

K. R. Stapelfeldt and M. W. Werner
Jet Propulsion Laboratory, California Institute of Technology, 4800 Oak Grove Drive, Pasadena, CA 91109

and

D. E. Backman
NASA–Ames Research Center, Moffett Field, CA 94035
Received 2006 April 10; accepted 2006 April 27

ABSTRACT

We have used the Infrared Array Camera (IRAC) on board the *Spitzer Space Telescope* to search for low-mass companions of the nearby debris disk star ε Eri. The star was observed in two epochs 39 days apart, with different focal plane rotation to allow the subtraction of the instrumental point-spread function, achieving a maximum sensitivity of 0.01 MJy sr^{-1} at 3.6 and 4.5 μm, and 0.05 MJy sr^{-1} at 5.8 and 8.0 μm. This sensitivity is not sufficient to directly detect scattered or thermal radiation from the ε Eri debris disk. It is, however, sufficient to allow the detection of Jovian planets with mass as low as $1 M_J$ in the IRAC 4.5 μm band. In this band, we detected over 460 sources within the 5.′70 field of view of our images. To test if any of these sources could be a low-mass companion to ε Eri, we have compared their colors and magnitudes with models and photometry of low-mass objects. Of the sources detected in at least two IRAC bands, none fall into the range of mid-IR color and luminosity expected for cool, 1 Gyr substellar and planetary mass companions of ε Eri, as determined by both models and observations of field M, L, and T dwarfs. We identify three new sources that have detections at 4.5 μm only, the lower limit placed on their [3.6]−[4.5] color consistent with models of planetary mass objects. Their nature cannot be established with the currently available data, and a new observation at a later epoch will be needed to measure their proper motion in order to determine if they are physically associated to ε Eri.

Subject headings: circumstellar matter — infrared: stars — planetary systems — stars: individual (ε Eridani)

Online material: color figure

1. INTRODUCTION

ε Eri (HD 22049, GJ 144, IRAS 03305−0937, HIP 16537), along with Vega, Fomalhaut, and β Pictoris, is one of the "Fabulous Four" nearby main-sequence stars found by the *Infrared Astronomical Satellite* (*IRAS*) to have a cool infrared excess (Gillett 1986). This excess is explained as thermal emission from cool dusty material. A careful analysis of the *IRAS* data has resolved the emitting regions for some of these stars, showing a disklike structure with a typical size of a few hundred AU, analogous to the Kuiper belt of our own solar system (Beichman 1987), but with a total mass of dust several orders of magnitude larger. Given that the timescales for the removal of primordial material (left over from the star formation process) are much shorter than the ages of these stars, it is believed that these structures—debris disks—are generated by the collisions between planetesimals and cometary activity. As such, debris disks are indirect evidence of planetary system formation (Backman & Paresce 1993).

With an age below 1 Gyr (850 Myr according to the most recent estimate by Di Folco et al. [2004], based on fitting VLTI angular diameter measurements with evolutionary models) and a K2 V spectral type, ε Eri is a relatively young star with a mass slightly lower than that of the Sun. The proximity of the system, 3.22 pc distance from the Sun (Perryman et al. 1997), offers the rare chance to study in detail the final phases of planetary system formation for a star similar to the Sun.

The debris disk of ε Eri was first imaged at 850 μm by Greaves et al. (1998) using the Submillimeter Common-User Bolometer Array (SCUBA) at the James Clerk Maxwell Telescope in Hawaii. The SCUBA images show a nearly face-on ring structure, extending as far as 35″ from the star, with a maximum of emission located at a radius of ∼18″. At the ε Eri distance this corresponds to a disk radius of over 100 AU, peaked at the distance of 60 AU from the star. The nearly face-on orientation of the disk is in agreement with measured projected rotational velocities (v sin i) indicating that the star is seen nearly pole-on (Saar & Osten 1997), with an angle of i ≈ 30° ± 15° for the pole of the star (deprojected adopting the rotational period of 11.68 days from Donahue et al. 1996).

The 1998 submillimeter map of ε Eri has revealed the presence of a few clumps of emission along the ring. Subsequent maps obtained in 2002 with SCUBA at 850 and 450 μm (Greaves et al. 2005), and at 350 μm with the SHARC II camera at the Caltech Submillimeter Observatory (D. J. Wilner & C. D. Dowell 2006, private communication), have confirmed the presence of some of these clumpy structures. Greaves et al. (2005) attempted to measure the orbital motion of the structures detected in their 1998 and 2002 SCUBA images, and preliminary results suggest a rotation of ∼6° counterclockwise (Greaves et al. 2005). The clumps have been interpreted as evidence for the presence of a substellar companion in resonant interaction with the dust: if confirmed, their measured motion would require an orbital radius of the resonant body of ∼20 AU. Sophisticated dynamic models of the submillimeter ring suggest an orbital radius for a Jupiter-mass planet between ∼40 AU (Ozernoy et al. 2000) and ∼60 AU

(Quillen & Thorndike 2002) from ϵ Eri ($12''$–$20''$ at ϵ Eri's distance) to have the required perturbing effect.

Radial velocity measurements have indeed discovered a Jovian class planet ($M \sin i = 0.86M_J$)[2] with an estimated semimajor axis of 3.4 AU and an eccentricity of 0.6 (Hatzes et al. 2000), orbiting with a period of $\approx$7 yr. This inner planet clearly cannot be responsible for the formation of the structures in the ϵ Eri debris disk, as it would not have any gravitational effect outside the inner $\sim$20 AU of the system (Moran et al. 2004), but it confirms the presence of a planetary system around the star.

Direct detection of ϵ Eri planetary companions has so far proved unsuccessful. Macintosh et al. (2003, hereafter M03) carried out near-IR Keck deep adaptive optics (AO) imaging that excluded the presence of planets with mass larger than $5M_J$ at spatial scales comparable to the radius of the dust structures in the debris disk (roughly in a $40''$ search radius). Proffitt et al. (2004, hereafter P04), while searching for disk-scattered light in the optical with the *Hubble Space Telescope* (*HST*), compiled a list of $\sim$60 objects between $12\rlap{.}''5$ and $58''$ in region E from ϵ Eri, none of which, in absence of a second epoch observation to measure proper motion, could be identified as a candidate substellar mass companion.

The Infrared Array Camera (IRAC; Fazio et al. 2004a) on board the *Spitzer Space Telescope* (Werner et al. 2004), thanks to its photometric system and unprecedented sensitivity in four photometric bands at 3.6, 4.5, 5.8, and 8.0 μm, can uniquely contribute to the search of substellar mass objects. Brown dwarfs and Jupiter-size planets are characterized by strong molecular absorptions features (CH_4, NH_3, H_2O) in the mid-IR wavelength range. The IRAC passband centered at 3.6 μm, in particular, is very sensitive to a deep methane absorption feature at 3.3 μm, while the band at 4.5 μm is largely free of molecular opacities. As a consequence, T dwarfs and gas giants have nearly unique colors in the IRAC bands and can be separated from other classes of astronomical sources in color-color and color-magnitudes diagrams, based on their IRAC photometry alone (Patten et al. 2004, 2006). Based on models by Burrows et al. (2003), a $5M_J$ planet at the distance of ϵ Eri will have a flux density of 1.3 mJy and will be easily detected by IRAC if the artifacts due to the presence of the bright star can be mitigated.

To take advantage of these unique characteristics of IRAC, we carried out deep imaging of ϵ Eri in all IRAC bands, as part of the Fabulous Four debris disk star *Spitzer* Guaranteed Time Observation (GTO) program (program ID 90). This program consists of the observation of Vega, Fomalhaut, β Pic, and ϵ Eri with all *Spitzer* instruments, in order to investigate the structure of their debris disks and to search for substellar companions. Results concerning the structure of the disks of Fomalhaut and Vega as seen by the Multiband Imaging Photometer for *Spitzer* (MIPS; Rieke et al. 2004) and the Infrared Spectrograph (IRS; Houck et al. 2004) have already been published (Stapelfeldt et al. 2004; Su et al. 2005). A paper based on IRS spectroscopy and MIPS imaging of ϵ Eri disk is in preparation (D. E. Backman et al. 2006, in preparation). We present here the result of the search for substellar companions around ϵ Eri made with IRAC. In § 2 we describe the IRAC observations and the data reduction, with particular emphasis on the technique adopted to remove the ϵ Eri starlight diffracted on the focal plane, to allow detection of faint sources as close as possible to the star. In § 3 we discuss our detection limits for disk-extended emission and for low-mass

companions. In § 4 we describe the results of our companion search and compare them with previous searches. Finally, we present our conclusions in § 5.

2. DATA ACQUISITION AND REDUCTION

Due to its proximity to the Sun, ϵ Eri is a very bright star in the mid-IR, with a 2MASS K magnitude of 1.76 (Cutri et al. 2003). Faint companions and diffuse circumstellar emission can be detected only after a careful subtraction of the bright central point source. *Spitzer* is specially suited for this task, thanks to the exceptional stability of its optics and pointing system that allows a precise measurement and reproducibility of its instrumental point-spread function (PSF). The IRAC observations for the whole Fabulous Four program were designed to maximize the ability of subtracting the stellar PSF.

Each star was observed in two epochs, typically 1 month apart, to take advantage of the different roll angle of the spacecraft, which is determined by the relative position of the spacecraft with the Sun. This strategy allows one to position the main features of the PSF (the diffraction spikes created by the tripod supporting the secondary mirror and a few artifacts created by the electronics), which are fixed with respect to the detector pixel grid, in different positions on the sky. This allows a complete coverage of the sky around each of the stars.

ϵ Eri was observed on 2004 January 9 (AOR 4876032) and 2004 February 17 (AOR 4876288). The roll angle offset between the two epochs is $20\rlap{.}°15$ clockwise. Each observation consisted of a sequence of 12 s full array frames (10.4 s integration time), dithered on the IRAC arrays on a 36 position Reuleaux triangle, using the small dither scale, with each position repeated 9 times. The total integration time was 3379.6 s (over 56 minutes) on-source, for each IRAC band. The source was set at the center of the array, where the PSF is cleaner from artifacts. The other Fabulous Four stars were observed with the same technique, and with a total integration timescaled according to the brightness of the source. A standard star (ϵ Indi) was also observed, with the same total integration time as ϵ Eri, to contribute to the measurement of the instrumental PSF. The total integration time was estimated on the basis of the sensitivity required to detect a Jupiter mass planet in the vicinity of ϵ Eri. The individual frame exposure time (10.4 s) was chosen because it allowed one to obtain a long total integration time divided in a manageable number of individual frames, while still avoiding excessive saturation of the star on the detector. Shorter frame times are available but could not be used because it would have been very inefficient to reach the required total integration time and the large field of view necessary to search for widely separated low-mass companions. The total field of view imaged in each band was $5\rlap{.}'78$, slightly larger than the IRAC field of view of $5\rlap{.}'21$, due to the dithering pattern.

Basic data reduction and calibration was done with the *Spitzer* Science Center (SSC) pipeline, versions S10.0.1 (first epoch) and S10.5.0 (second epoch). The IRAC pipeline returns the individual exposures calibrated in physical units of surface brightness. This calibration is valid only for point sources, as it was obtained by matching the flux of standard stars modeled by Cohen et al. (2003) within an aperture of $12\rlap{.}''2$. Note that point source photometry with different sets of apertures and sky annuli and the photometry of extended sources requires the use of appropriate aperture corrections. These aperture corrections and the other parameters used in the absolute photometric calibration (including the "FLUXCONV" factors used to convert the raw data in DN s^{-1} into the science calibrated data in MJy sr^{-1}) are listed in Table 1.

---

[2] The deprojected mass has not been determined yet, but there is an ongoing effort by Benedict & McArthur (2004) to derive it from the astrometric wobble of the star measured with the *HST* Fine Guidance Sensors.

<div align="center">

TABLE 1

IRAC PHOTOMETRIC CALIBRATION

</div>

ITEM	IRAC BAND			
	3.6 μm	4.5 μm	5.8 μm	8.0 μm
Isophotal λ (μm)..	3.458	4.492	5.661	7.870
FLUXCONV [(MJy sr^{-1})/(DN s^{-1})]	0.1125	0.1375	0.5913	0.2008
Saturation limits (DN)	30,000	35,000	45,000	50,000
Saturation limits (MJy sr^{-1})	320	460	2560	970
Infinite aperture corrections...........................	0.94	0.94	0.63	0.69
2″.4 aperture corrections[a]...............................	1.213	1.234	1.379	1.584
Zero-point magnitudes[b]	19.46	18.97	18.38	17.56
F_ν(Vega) (Jy)...	277.5	179.5	116.5	63.1

NOTE.—Based on IRAC Data Handbook (2004).

[a] For sky annulus with 2″.4 and 7″.2 inner and outer radii.

[b] For pixel size 0″.4 pixel^{-1}, including 2″.4 aperture correction.

For each epoch separately, we have created a mosaic combining the individual frames, using the SSC Mosaicer MOPEX on a final grid with a pixel scale of 0″.4 pixel^{-1} (a factor of 3 smaller than the original IRAC pixel scale of $\approx$1″.22 pixel^{-1}) to leverage the high coverage for a better sampling of the PSF. We have chosen to maintain the same orientation in the final mosaic as the individual frames to have the PSF features oriented with the same angle in the mosaics of the two epochs. Cosmic rays and other outliers have been removed using the MOPEX temporal outlier module. This procedure was repeated identically for all Fabulous Four sources, including the standard star, in all epochs.

2.1. *PSF Subtraction*

Figure 1 shows the Fabulous Four program PSF we have derived by combining the mosaics of Vega (two epochs) and ϵ Indi (one epoch). Note that Vega itself is a star surrounded by a debris disk, but the infrared excess in IRAC bands is too small to be detectable by IRAC (Su et al. 2005). Vega can thus be considered as a point source for the purpose of building our PSF. The three mosaics have been shifted by matching the position of the unsaturated diffraction spikes, rescaled according to the relative brightness of Vega and ϵ Indi, and then co-added. The final PSF is clean of background stars that have been σ-clipped in the co-adding phase.

A special version of the PSFs we have generated for this project, which combines all the stars of the Fabulous Four program with the exclusion of β Pic (whose debris disk is indeed extended at IRAC wavelengths), is available at the SSC Web site[3] for different pixel scales. These public PSFs also include an unsaturated core derived from the observation of faint standard stars as part of the IRAC photometric calibration project. A paper describing the construction of these PSFs and their main characteristics is in preparation (M. Marengo et al. 2006, in preparation).

It is clear from Figure 1 that the IRAC PSF has a lot of structures and artifacts that are the main limiting factor for observing faint emission around bright sources. These artifacts cover the whole area of the IRAC arrays and can be divided in two categories. The six diffraction spikes (each of them composed of two initially braided and then diverging individual spikes), the smooth extended PSF tails, the diffraction rings and the PSF "ghosts" ("filter ghosts," small "ringlike" and "crosslike" structures at the left of the PSF peak at 3.6 and 5.8 μm and the right at 4.5 and 8.0 μm, and "beam splitter ghosts," fainter structures

below the 5.8 and 8.0 μm PSF peaks) are part of the "optical PSF." These structures are linear in intensity with the fluency of the source (product of its surface brightness with the integration time) and can thus be easily subtracted even with a PSF derived from stars of different brightness than the source, as long as the PSF stars are observed with the same dither pattern and in the same position on the IRAC detectors (the position of the ghosts and the orientation of the diffraction spikes does depend on the array position). The negative columns ("column pull-down," white area in Fig. 1) and the positive fencing pattern ("muxbleed," visible in Fig. 2 after PSF subtraction) in the 3.6 and 4.5 μm bands, the large positive "crosses" (vertical and horizontal "banding") and the saturated multiple "echos" on the right of the saturated core ("bandwidth effect") in the 5.8 and 8.0 μm bands are instead "electronic artifacts" generated by the detector and the readout electronics and artifacts resulting from internal scattering of IR light within the detectors. The column pull-down also affects the 5.8 and 8.0 μm bands but can be hidden below the stronger banding. The electronic artifacts are not linear with the source fluency and can only be subtracted using a PSF obtained from stars with the same signal as the source.

The PSF that we have derived from Vega and ϵ Indi is only effective for subtracting the optical structures of the PSF. To eliminate the electronic artifacts it is necessary to use an alternative approach, based on the observation of ϵ Eri in two epochs, with two different roll angles. By using the second epoch as a PSF model for the first epoch (a PSF with exactly the same fluency of the source), we can effectively subtract the optical PSF *and* the electronic artifacts while preserving the background sources that are rotated in the two epochs with respect to the PSF. In a two-epoch subtracted frame the background sources from one epoch will be positive, and the ones from the other epoch will be negative. The tradeoff for this technique is that for a very crowded field there is the risk of aliasing "positive" with "negative" sources when they superpose by chance, due to the rotation of the field.

To have the best possible coverage of the sources in the ϵ Eri field, we have applied both PSF subtraction techniques in all IRAC bands. For each band we have thus produced four PSF-subtracted frames: (1) first epoch subtracted with the PSF, (2) second epoch subtracted with the PSF, (3) first epoch subtracted with the second epoch, and (4) second epoch subtracted with the first epoch (epochs 3 and 4 are of course the same, except for the orientation on the sky and the sign).

Figure 3 shows an example of the two PSF subtraction techniques (*right panels*) compared with the original images before

---

[3] See http://ssc.spitzer.caltech.edu/irac.

Fig. 1.—IRAC PSF at (*a*) 3.6 μm, (*b*) 4.5 μm, (*c*) 5.8 μm, and (*d*) 8.0 μm. The PSF is shown in inverted logarithmic color scale, from zero intensity (*white*) to saturation level (*black*). The size of each panel is the same as the IRAC field of view (∼312″). The main artifacts are marked. The beam splitter ghosts at 5.8 and 8.0 μm are the faint kinks visible along the vertical banding where the arrows point. Note that there is also column pull-down at 5.8 and 8.0 μm, which is, however, not visible due to the predominant effect of the banding. Muxbleed is also present at 3.6 and 4.5 μm and can be seen after PSF subtraction in Fig. 2. Note that the horizontal spikes at 5.8 and 8.0 μm are hidden below the banding.

PSF subtraction (*left panels*). The top right panel shows the epoch 2 image subtracted with the PSF: note the remaining cross due to imperfect subtraction of the "electronic" artifacts. The bottom right panel shows the second epoch image subtracted from the first: note the better subtraction of the electronic artifacts, but the occurrence of aliasing for some of the field sources. Both PSF subtraction methods are able to remove most of the ε Eri light scattered by the PSF and bring forth the numerous fainter sources in the field. Limits to this technique due to residual noise after the PSF subtraction are described in the following section.

The PSF subtraction technique described here allows one to measure the brightness of ε Eri with considerable precision, by determining the scaling factor between the ε Eri image and the PSF (which is normalized, by construction, as the calibrated image of Vega). This scaling factor is determined by the fitting routine to better than 1%, which translates into an accuracy of ∼0.01 mag. The measured magnitudes, in each epoch, are listed in Table 2 (the conversion from magnitudes to fluxes uses the IRAC Vega fluxes also reported in the IRAC Data Handbook 2004). Note

that there is no photometric variation between the two epochs, with the exception of the ∼2.7% change in the 5.8 μm flux (which is, however, within 3 σ of the estimated photometric error).

3. SENSITIVITY LIMITS FOR EXTENDED AND POINT SOURCES

The PSF subtraction methods described in § 2 are able to remove most of the ε Eri light scattered on the IRAC arrays by the *Spitzer* optics and the detector electronics. The subtraction, however, leaves a number of artifacts and residual noise that limits our capability to search for faint companions and extended structures. These residuals are especially strong in close proximity to the star, precluding the search for planetary companions in the inner ε Eri system.

Figure 4 shows the radial profiles of ε Eri before (*thin line*) and after (*thick line*) PSF subtraction, along a wedge with position angle 120° and width 40° (positioned to avoid diffraction spikes and electronic artifacts). Note the presence of a background pedestal, in part due to an imperfect subtraction of the dark frames, and in part due to an electronic pedestal produced when a bright
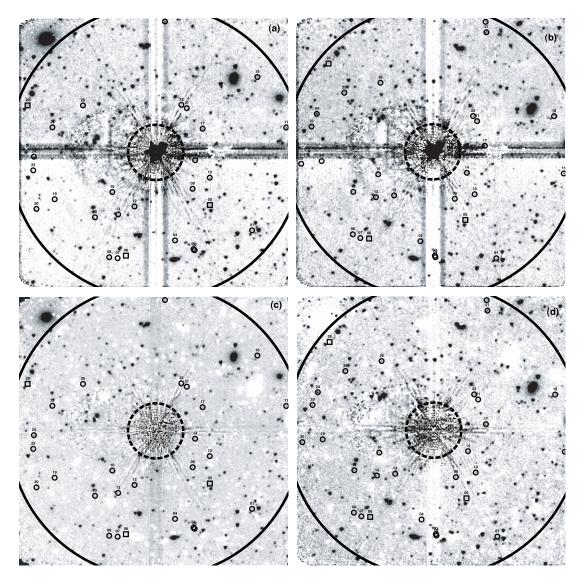
Fɪɢ. 2.—PSF-subtracted IRAC 4.5 μm images of ε Eri background field: (*a*) Epoch 1 subtracted with the PSF, (*b*) epoch 2 subtracted with the PSF, (*c*) epoch 1 subtracted with epoch 2, and (*d*) epoch 2 subtracted with epoch 1. The figure uses an inverted linear color scale from background level to 0.1 MJy sr^{-1}. The inner circle marks the maximum radius of the submillimeter ring (112 AU, corresponding to 35″ at the ε Eri distance). The outer circle marks the distance of 600 AU. Circle points mark the location of point sources for which only a marginal detection ($\lesssim 5\ \sigma$) at 3.6 μm is available. The three sources with no detection at all at 3.6 μm are indicated with square points.

source is incident on the detector. This background pedestal is particularly strong in IRAC images containing bright sources, as is the case with ε Eri, and is larger at longer wavelengths. The pedestal level in our observations was ∼0.1, 0.2, 2.5, and 6.0 MJy sr^{-1} at 3.6, 4.5, 5.8, and 8.0 μm, respectively, and was successfully removed from the PSF-subtracted images (but not from the profiles shown in Fig. 4) during PSF subtraction by adding a constant value to the scaled PSF, even though a small residual slope was left in the final 5.8 μm images.

The IRAC arrays become severely nonlinear when the signal exceeds the ∼30,000–50,000 DN range (see Table 1). Above this limit the image is rapidly saturated. This effect can be observed in the radial profiles as a surface brightness depression in the inner 5″–7″ (16–22 AU), where all signal is lost, making the core of the star resemble a "donut." Outside this radius the PSF profiles rapidly fall, even though the residuals after PSF subtractions are still high within ∼14″ from the star (∼45 AU). These residuals are mainly due to the high photon noise of the bright source, the buildup of strong latents during the long total integration, and the intrinsic limitations in the PSF construction

method: even small changes in the dither pattern, combined with the undersampling of the IRAC PSF (especially severe at 3.6 and 4.5 μm), can cause small but significant deviations in the PSF profiles that result in elevated residual noise where the PSF signal is stronger. Outside a ∼14″ radius the PSF subtraction is, however, very effective for lowering the PSF signal to the photon noise level.

3.1. *Limits on the Debris Disk Detection*

P04 have used the STIS CCD camera on *HST* to search for an optical counterpart of the submillimeter disk in scattered light. The result of their search was inconclusive, but they set an upper limit of 25 mag arcsec^{-2} for the optical surface brightness of the dust at the distance of 55 AU from the star (17″, roughly the distance where the millimetric disk emission peaks), within the "clear aperture" wide spectral bandpass of the STIS camera (from 0.2 to 1.02 μm). At the nominal wavelength of 0.7 μm, this limit corresponds to a surface brightness of 0.011 MJy sr^{-1}.

Given that the spectral energy distribution of a K star like ε Eri peaks in the near-IR, the intensity of the light scattered from the
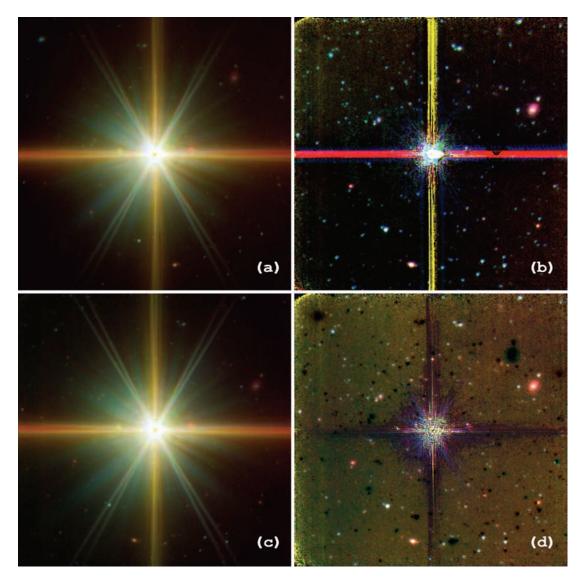
FIG. 3.—ϵ Eri before (*left*) and after (*right*) PSF subtraction. In the color composite, blue is 3.6 μm, green is 4.5 μm, yellow is 5.8 μm and red is 8.0 μm. Note the rotation of the field of view between (*a*) epoch 1 and (*c*) epoch 2. (*b*) Epoch 2 subtracted with the PSF constructed from Vega and ϵ Indi. (*d*) Epoch 2 subtracted with epoch 1. The left panels are shown in logarithmic color scale, while the PSF-subtracted images are shown in linear scale from -0.5 to 1.0 MJy sr^{-1}. The total field of view is 334″.

disk rapidly decreases at wavelengths longer than 1 μm, at least until the thermal emission of small grains starts to be significant (for $\lambda \gtrsim 10$ μm). This means that at IRAC wavelengths the total disk surface brightness will be very small. P04 have developed a model of the disk surface brightness based on a previous model by Li et al. (2003), fitting the 850 μm and *IRAS* emission and in-

cluding the contribution from scattered optical light. This model, which assumes the presence of highly porous particles, and a rather flat grain size distribution from 1 μm to 1 cm, predicts that the surface brightness of the disk at 3.6 μm and at the distance of 55 AU would be less than 0.002 MJy sr^{-1}, and even lower in the other IRAC bands (see P04, Fig. 11). This surface brightness is too small to be detected in our PSF-subtracted images.

Figure 5 shows the sensitivity of our images for extended sources, after subtraction of the ϵ Eri starlight. We initially computed the rms noise in a running boxcar of 4″ size for the PSF and two-epochs subtracted images, obtaining four maps for each IRAC band. The four maps differ in that the residuals of the PSF subtraction, and thus the residual noise, depend on the PSF subtraction method and on the rotation of the field with respect to the array coordinates. Since we are interested in the best case sensitivity achievable combining both epochs and both PSF subtraction methods, we have constructed a final map by taking the minimum rms value, in each pixel, of the individual maps. We have then corrected the minimum rms maps for the "infinite aperture correction" necessary to recalibrate the maps for the case of extended sources (listed in Table 1).

TABLE 2
ϵ ERI IRAC MAGNITUDES AND FLUXES

		2004 January 9		2004 February 17	
IRAC Band	λ_0[a] (μm)	Magnitude[b]	Flux[c] (Jy)	Magnitude[b]	Flux[c] (Jy)
[3.6]..............	3.548	1.59	63.9 ± 0.3	1.59	64.1 ± 0.4
[4.5]..............	4.492	1.66	39.1 ± 0.2	1.65	39.2 ± 0.2
[5.8]..............	5.661	1.61	26.5 ± 0.2	1.64	25.8 ± 0.2
[8.0]..............	7.870	1.60	14.5 ± 0.1	1.59	14.6 ± 0.1

[a] IRAC nominal wavelengths from the IRAC Data Handbook (2004).
[b] Magnitudes accurate to ±0.01 mag.
[c] Using IRAC Vega fluxes from the IRAC Data Handbook (2004).

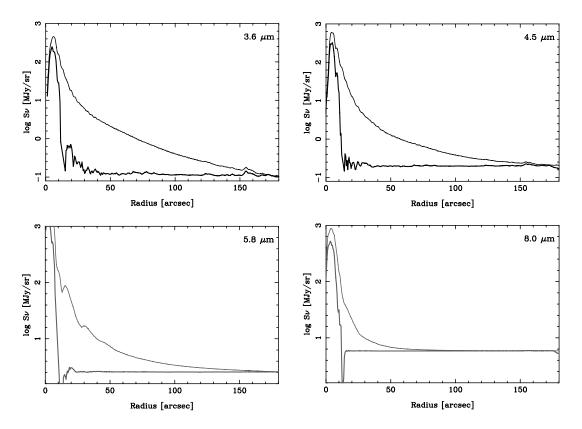FIG. 4.— ϵ Eri (epoch 2) radial profiles before (*thin line*) and after (*thick line*) subtraction with the IRAC PSF in the four IRAC bands. The profile is a circular average within a wedge of $40°$ width, with a position angle of $120°$ from the vertical, clockwise (to avoid diffraction spikes and other artifacts). The background pedestal level has not been subtracted from the profiles presented in this figure (even though it is removed from the PSF-subtracted images used in the rest of the analysis).

The contours show that the residual rms noise increases closer to the star, as expected, and along the main PSF artifacts (diffraction spikes and electronic artifacts). The large oval shape at the left of the star at 4.5 μm is enhanced noise due to a pupil ghost. At a distance of 55 AU from the star the sensitivity is greater than 1 MJy sr^{-1} in all channels, making it impossible to test the accuracy of the P04 model. Even as far as $1'$ from the star, the maximum sensitivity (0.01 MJy sr^{-1} at 3.6 and 4.5 μm and 0.05 MJy sr^{-1} at 5.8 and 8.0 μm) is still not sufficient to detect the scattered light from the disk.

The P04 model predicts a total flux of 0.12, 0.14, 0.19, and 0.40 mJy at 3.6, 4.5, 5.8, and 8.0 μm. Using a simple model of a thin ring with solid silicate and organic grains with a size distribution similar to the interstellar medium (Mathis et al. 1977) but ranging from 1.75 μm to 5 m, Sheret et al. (2004) found a larger flux of 1.7, 1.5, 0.97, and 0.53 mJy in the IRAC bands. In both cases the predicted fluxes are much smaller than the accuracy of our IRAC photometry (see Table 2), and the expected infrared excess from the disk over the photospheric emission cannot be detected by our measurement.

3.2. *Limits on Low-Mass Companion Detection*

Models shows that, at least in the case of a faint debris disk like the one around ϵ Eri, the detection of scattered light from the circumstellar dust is beyond the sensitivity limits of our PSF-subtracted images. The main goal of IRAC imaging, however, is the search for faint companions with substellar mass. From the profiles shown in Figure 4 it is clear that we have no point source sensitivity closer than $\sim14''$ (45 AU) from the star because of saturation, nonlinearity, and high photon noise preventing usable PSF subtraction very close to the star. This rules out the possibility of searching for the radial velocity planet at 3.2 AU, which would be well within the saturated area in our images. A different story, however, concerns the possibility of detecting the planet whose presence at a distance between 40 and 60 AU ($12''$–$20''$) is predicted by some dynamic models of the observed clumps in the debris disk. Even though such a planet has been unsuccessfully located by M03, the superior sensitivity of IRAC and the photometric system more suited to the observation of low-mass objects may give us the chance of detecting this body if it exists and if its mass is above our detection limits. The wide field of view of the IRAC maps (covering an area with size over 1200 AU around the star) also allows us to search for widely separated planets that may have been ejected from the system, due to planet-planet interactions (Ford et al. 2001), in case the total protoplanetary disk mass was not sufficient to dampen the eccentricity of planets forming in the system.

Since the discovery of brown dwarfs (Becklin & Zuckerman 1988; Nakajima et al. 2005), several groups have started to compute detailed model atmospheres of substellar mass objects to predict what would be their emission spectra and luminosity. More recently, these models became very sophisticated, including large lists of molecular and alkali opacities, dust formation and settling, improved treatment of line pressure broadening, and the effects of water clouds and ice formation, enabling them to compute reliable spectra extending in the IR domain. Figure 6 shows a family of such models, computed by Burrows et al. (2003) for 1 Gyr old substellar objects with mass from $1M_J$ to $25M_J$. The model spectra are shown in the wavelength range covered by the IRAC photometric system and have been rescaled for the distance of ϵ Eri. As mentioned in § 1, the spectrum of substellar objects in the IRAC bands is modulated by deep CH_4 and H_2O absorption features. Methane absorption is particularly strong in the 3.6 μm IRAC band, where it can depress
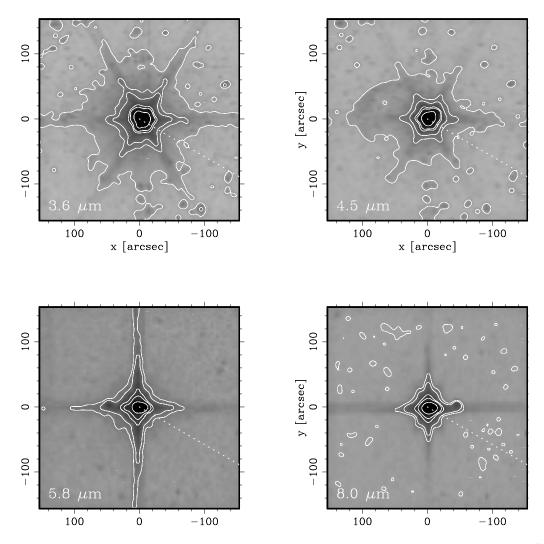
Fig. 5.—Sensitivity maps, in array coordinates, computed as the rms noise of the PSF-subtracted images, estimated in a running boxcar of size 4″. The contours show the rms noise of 5, 1, 0.5, 0.1, 0.05, and 0.01 MJy sr^{-1}, with the highest noise level at the center. The dotted line indicates the direction of the cut used to plot the radial profiles in Figs. 4 and 7.
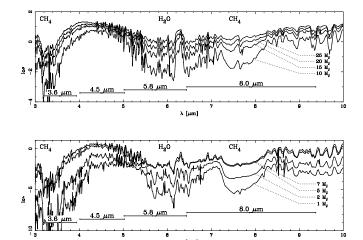

Fig. 6.—Model spectra of gas giants and brown dwarfs from Burrows et al. (2003), computed for 1, 2, 5, 7, 10, 15, 20, and 25 M_J 1 Gyr bodies. The predicted flux density has been rescaled for the distance of ϵ Eri. The main spectral features in the IRAC bands are produced by molecular absorption of CH_4 (in the 3.6 μm and 8.0 μm bands) and H_2O (in the 5.8 μm band). The band at 4.5 μm is relatively free of absorption and is where Jupiter-size planets would appear brighter.

the flux by a few orders of magnitude below the continuum, with increasing strength for decreasing temperature (and thus decreasing mass, for a fixed age). A second broad methane feature is present within the 8.0 μm band, while water absorption affects the flux around 5.8 μm. The 4.5 μm IRAC band, however, is relatively free of molecular absorption and thus offers the best chances of detection for molecular rich, cool substellar objects.

We have estimated the magnitude and colors of the atmosphere models presented in Burrows et al. (2003) in the IRAC photometric system by integrating each model with the IRAC bandpasses, normalized by the flux of Vega:

$$m_{\mathrm{band}} = -2.5 \log \frac{\int_{\mathrm{band}} F_\nu(\lambda) R_\nu(\lambda) \lambda \, d\lambda}{\int_{\mathrm{band}} F_\nu^{\mathrm{Vega}}(\lambda) R_\nu(\lambda) \lambda \, d\lambda}, \quad (1)$$

where $F_\nu(\lambda)$ is the model spectrum, $F_\nu^{\mathrm{Vega}}(\lambda)$ is the model spectrum of Vega, derived by Robert Kurucz for Martin Cohen (this is the same model used for the absolute photometric calibration of IRAC), and $R_\nu(\lambda)$ is the IRAC spectral response curve from the IRAC *Spitzer* Science Center Web site[4] (2004 August 9 version).

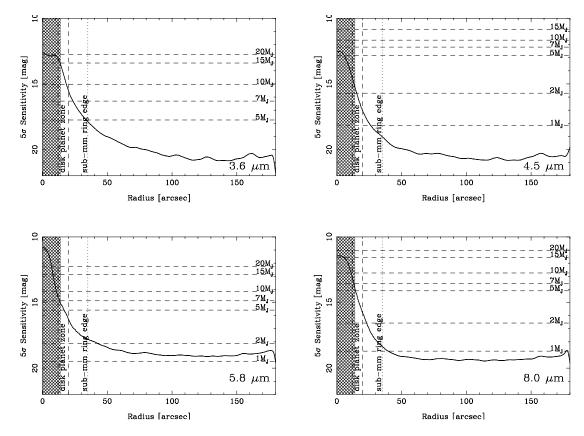[4] See http://ssc.spitzer.caltech.edu/irac/spectral_response.html.

FIG. 7.—Detection limits for giant planets and brown dwarfs based on models computed by Burrows et al. (2003). The solid line shows the 5 σ point source sensitivity (within an aperture of 2″4 radius) derived from the rms maps in Fig. 5, along a cut with position angle 120° and 40° width. The cross-hatched region within a radius of 14″ (45 AU) from the star should be excluded because of saturation and high residual noise after PSF subtraction. The dashed vertical lines show the region where dynamic models predict the presence of a resonant body (between 40 and 60 AU), while the dotted vertical line marks the outer radius of the submillimetric ring at 35″ (112 AU).

The predicted magnitudes are shown in Figure 7 and compared with the 5 σ point source sensitivity of our PSF-subtracted images along the same radial cut used in Figure 4. We have derived the point source sensitivity from the maps in Figure 5 by converting the rms noise into noise equivalent flux density (NEFD) inside an aperture of 2 IRAC pixel radius (2″4):

$$m^{5\,\sigma}(x,\ y) = -2.5 \log \left[\frac{5\mathrm{NEFD}(x,\ y)}{F_{\mathrm{Vega}}} \right], \qquad (2)$$

and

$$\mathrm{NEFD}(x,\ y) = 2.3504 \times 10^{-5} r_A \sqrt{\pi}(\mathrm{pixel\ scale})^2$$
$$\times \mathrm{acorr}(r_A)\mathrm{rms}(x,\ y), \qquad (3)$$

where $m^{5\,\sigma}$ is the point source sensitivity in magnitudes at the $(x,\ y)$ coordinates in the PSF-subtracted images, rms$(x,\ y)$ is the sensitivity map shown in Figure 5, F_{Vega} is the flux of Vega in the IRAC bandpasses reported in the IRAC Data Handbook (2004), and the other quantities are geometrical factors necessary to convert surface brightness into flux, and include the aperture radius r_A, the pixel scale of the PSF-subtracted images (0″4 pixel^{-1}), and the aperture correction acorr(r_A) for 2 IRAC pixel apertures, also from the IRAC Data Handbook (2004), listed in Table 1.

Figure 7 shows that the IRAC band most sensitive to detect cool companions is indeed the one at 4.5 μm. Outside the area where the image is contaminated by saturation, nonlinearities and photon noise from the central bright star (cross-hatched in the figure), our PSF-subtracted images are sensitive to Jupiter mass planets. Just inside the inner edge of the ring we are sensitive to planets with a mass of $\simeq 1M_J$, and below $1M_J$ in the area outside the debris disk. The strong methane absorption in the 3.6 μm band increases considerably the minimum detectable mass at this wavelength, so much that in the region inside the disk where dynamic models suggest the presence of planets gravitationally perturbing the disk, we are only sensitive to bodies with mass larger than $7M_J$. The sensitivity in the two remaining IRAC bands (5.8 and 8.0 μm) is intermediate between these two extreme cases. Note that, with the exception of the 3.6 μm band, outside a radius of 45 AU our PSF-subtracted images are at least a factor of 2 more sensitive in terms of mass than the Keck K-band images in M03, and at least 5 times more sensitive outside the submillimeter ring.

4. COMPANION SEARCH

Even though ϵ Eri is relatively far from the Galactic plane, the field around the star shows a large number of background sources. The challenge is determining whether any of them can be a gravitationally bound low-mass companion, instead of a faint background star or galaxy, or an artifact from the PSF subtraction. A similar search made by P04 in the optical concluded that most of the detection were, in fact, background galaxies. Given the sensitivity of IRAC to red extragalactic objects, we should expect a similar result.

As mentioned above, the colors of substellar objects in the IRAC photometric system are very peculiar. The colors of brown dwarfs and giant planets at the distance of ϵ Eri can be estimated from Burrows et al. (2003) models, as described in § 3.2. For all background sources having good photometry in at least two or three IRAC bands, it is thus possible to investigate their nature

on the basis of color-color and color-magnitude diagrams. Planets below $5M_J$, however, may be detected in only one IRAC channel, at 4.5 μm, because of the lower sensitivity at 5.8 and 8.0 μm, and the deep methane absorption feature depressing their 3.6 μm flux below our sensitivity level. Given that our two epochs are too close in time to allow for proper motion measurements, for these "3.6 μm dropout" sources a new observation at a later epoch is needed to check if they are comoving with the ϵ Eri system.

4.1. *Source Detection and Photometry*

The PSF subtraction procedure leaves behind a large number of point-source-like artifacts that can easily confuse the detection algorithms available in most photometry packages. In particular, analysis based on the shape of the point sources by Gaussian or PSF fitting of all structures above a certain threshold would reject a large number of valid sources whose shape has been distorted by the proximity with the PSF artifacts, or by a nearby "aliasing" source in the two epoch-subtracted frames. Given our requirement to be inclusive, not to miss the proverbial "needle in the haystack" that would be a planet orbiting ϵ Eri, we have relaxed our requirements starting with a list including *any* detection with S/N $\gtrsim 5$ within an aperture of 2″.4 radius. We have then selected the real from the spurious sources by visually inspecting each detection and by comparing the two epochs and the results from the two different PSF subtraction methods described in § 2.1. With this procedure we have obtained a list of 467 sources between 12 and 20 mag, reliably detected in at least one epoch at 4.5 μm within the IRAC field of view.

Fazio et al. (2004b) shows that, outside the plane of the Galaxy, most of the sources detected by IRAC with a magnitude $\gtrsim 13$ at 4.5 μm are background galaxies. Table 1 in that paper shows that the total number of background galaxies with 4.5 μm magnitudes between 15 and 20 within the area of our maps is $\sim$920. This is consistent with our number of detections, taking into account the large area at the center of our PSF-subtracted images where our sensitivity limits is well below the 20th magnitude because of the high PSF subtraction residuals.

For source detection and photometry we have used the package "PHOTVIS" developed by R. Gutermuth (Gutermuth et al. 2004), based on the "APER" aperture photometry package part of the IDL "ASTROLIB" library. The size of the aperture was set to 2″.4, with a sky annulus with inner and outer radii of 2″.4 and 7″.2. To convert the mosaic data (in MJy sr^{-1} surface brightness units) into magnitudes we have derived zero-point magnitudes based on the Vega fluxes adopted for the camera's absolute calibration, listed in Table 1.

The uncertainty of each photometric measurement was estimated as the sum in quadrature of the scatter in the sky values, the uncertainty in the mean sky brightness, and the random photon noise on source (estimated from the source counts converted in electrons). Note that this error analysis tends to underestimate systematic errors due to imperfect subtractions of the PSF and PSF artifacts that alter the sky level and introduce non-Gaussian noise.

We have then merged the individual source lists in each band and PSF subtraction method. In each IRAC band we have averaged the individual photometry in the two epochs and PSF subtractions, weighted on their S/N. Typical uncertainties of the final photometry are $\sim$0.05 mag at 3.6 and 4.5 μm, and $\sim$0.1 mag at 5.8 and 8.0 μm. Sources close to ϵ Eri or along PSF subtraction artifacts may have a larger uncertainty in one of the two epochs, depending on the PSF subtraction method. We have checked the consistency of the photometry of sources detected in both epochs and found that it is generally within the error margin, except
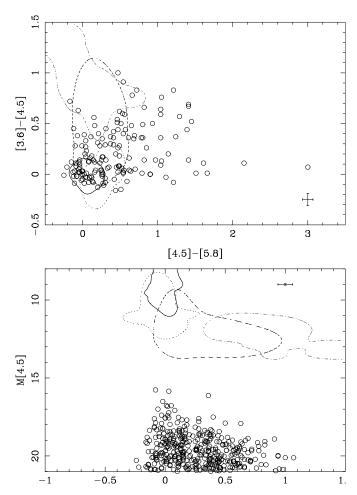

Fig. 8.—Color-color and color-magnitude diagrams of all point sources detected in the field around ϵ Eri. The contours are the region selected with the kNN method for M dwarfs (*solid line*), L dwarf (*dotted line*), early T dwarfs ($T < 5$, *dashed line*), and late T dwarfs ($T \gtrsim 5$, *dot-dashed line*). Note that many sources have the right colors to be M, L, or T dwarfs, but none of them has the correct brightness to be an M, L, or T companion of ϵ Eri, according to the colors and magnitudes of field M, L, and T dwarfs from Patten et al. (2006).

when a PSF artifact or source aliasing is present. In these cases, we assume an uncertainty of $\sim$0.2 mag, representative of the maximum spread observed in the photometry of sources detected in both epochs in at least two IRAC bands.

4.2. *Color-Color and Color-Magnitude Diagrams*

The top panel of Figure 8 shows the [3.6]$-$[4.5] versus [4.5]$-$[5.8] color-color diagram of the sources detected in all three bands. Note that many of the sources are clumped around zero colors, indicating that they are regular background stars. A significant number of sources, however, have one or both colors red: this is expected for extragalactic sources having significant PAH emission in the longer wavelength IRAC bands, or redshifted galaxies (Huang et al. 2004; Barmby et al. 2004). The bottom panel shows the [3.6]$-$[4.5] color versus the 4.5 μm absolute magnitude that the sources detected in both 3.6 and 4.5 μm bands would have if they were at the same distance (3.22 pc) as ϵ Eri.

The contours plotted on the figure enclose the locations where sources with the colors of field M, L, and T dwarfs are located in the diagram. These contours have been derived from data collected as part of the IRAC Guaranteed Time observations of M, L, and T dwarfs (Patten et al. 2004, 2006), using a variation of

the weighted *k*-Nearest Neighbor Method (*k*NN; Fix & Hodges 1951) adapted for astronomical applications. The method, commonly used in diagnostic medical studies, is a multivariate analysis very effective in the automated classification of items in different groups. In this work we have used $k = 3$ (third nearest neighbor) and a Gaussian kernel to bias the metric toward the first nearest neighbor. Sources inside each region differ from the class templates (the M, L, and T field stars observed by Patten et al. 2006) by less than 1 σ error in photometry or color. A detailed description of this method will be given in a separate paper (M. Marengo & M. C. Sanchez 2006, in preparation).

The top panel of Figure 8 shows that many of the sources detected around ϵ Eri have colors compatible with the colors observed for field M, L, and T dwarfs (Patten et al. 2006). The bottom panel of the same figure, however, shows that all the sources detected at least at 3.6 and 4.5 μm are much fainter than all the field M, L, and T dwarfs in the Patten et al. (2006) sample. Although the observed field M, L, and T dwarfs have a range of masses and ages that may not be appropriate for ϵ Eri, lower mass brown dwarfs and planets at a given [3.6]−[4.5] color cannot be much fainter than the $M_{4.5}$ range shown for the field objects. The reason is that the radii of ∼1 Gyr brown dwarfs and planets span a relatively small range of values and are relatively constant independent of age and mass (Burrows et al. 1997; Chabrier & Baraffe 1997). Hence, their luminosity depends primarily on temperature and, consequently, color.

This is demonstrated in Figure 9 by the Burrows et al. (2003) models of 1 Gyr old brown dwarfs and giant planets. The large area covered by the *k*NN contours is determined by the large systematic error we have assumed for the models, approximately as large as the color separation between the models of individual mass. This is a prudent assumption, in our requirement to be inclusive, given that these models have never been directly tested toward real extrasolar planets. Even so, none of the detected sources possess the right combination of colors and magnitudes to be a candidate planet or T dwarf, as all the planet models have a [3.6]−[4.5] color much redder, and a [4.5]−[5.8] color much bluer (due to H$_2$O absorption at 5.8 μm), than the sources detected in at least two IRAC bands.

4.3. *The* 3.6 μm *Dropout Sources*

Figure 9 shows that a planet with $5M_J$ would have a 4.5 μm absolute magnitude of ∼15.3 and a [3.6]−[4.5] color of 4.9. This means that the 3.6 μm magnitude of that planet at the distance of ϵ Eri would be 20.2, which is below our detection limit. Such a planet can be detected in the 4.5 μm images but would drop out from our 3.6 μm images. Bodies with mass below ≲$5M_J$ cannot be found on the basis of their color with the *k*NN method described in § 4.2, and their identification should rely on proper motion measurements.

The time lag between our two epochs, however, is too short to yield a measurable shift of ϵ Eri and any companion. The proper motion of ϵ Eri is of $-0\rlap{.}''977$ yr^{-1} in R.A. and $0\rlap{.}''018$ yr^{-1} in decl. (Perryman et al. 1997), which means that during the 39 days between the two epochs the star moved by ∼$0\rlap{.}''1$. This is a factor of 2 less than our best-case centroiding accuracy (∼$0\rlap{.}''2$ at 4.5 μm, where the IRAC pixel scale has the optimal PSF sampling). Comparison with other catalogs is not possible, with the exception of the few sources in common with the P04 and M03 surveys, as described in the next section.

Table 3 lists all the sources, within a radius of 600 AU (approximately the area covered by our images) that have a 5 σ detection at 4.5 μm but are not detected at the 5 σ level at 3.6 μm.
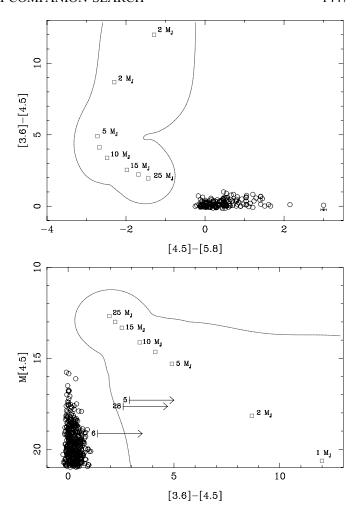

Fig. 9.—Color-color and color-magnitude diagrams of 850 Myr giant planet model tracks from Burrows et al. (2003), compared with the sources detected in the ϵ Eri field. Square points denote the colors and magnitudes of model planets with mass from $25M_J$ to $1M_J$. The solid line encloses the region in the diagrams where candidate planets may be found, according to our *k*NN method. None of the sources detected at both 3.6 and 4.5 μm has the correct colors and magnitudes predicted by Burrows et al. (2003) models. The arrows indicate the photometry and colors of the three 3.6 μm dropout sources listed in Table 3.

Most of these sources do have, however, a marginal 3.6 μm detection, and their colors (even allowing for the large uncertainties in their 3.6 μm photometry) suggest that they are red background galaxies. Only three sources are completely undetected at 3.6 μm. Their 4.5 μm fluxes and [3.6]−[4.5] colors (estimated from the 3.6 μm sensitivity limit in Fig. 5) are compatible with the colors and magnitudes of planets with masses ≲$3M_J$ (sources 5 and 28 in Table 3) and ≲$2M_J$ (source 6 in Table 3), but not with faint redshifted galaxies (which typically have [3.6]−[4.5] ≲0.5). J. Huang et al. (2006, personal communication) found that out of 7.3×10^4 sources detected by IRAC in an area of $2° \times 10'$ with a 3 hr exposure, only six have a 4.5 μm magnitude between 17.5 and 20, and [3.6] − [4.5] > 1.5. It is thus very unlikely to have three such sources within a single IRAC field of view. A careful inspection of the individual 4.5 μm PSF-subtracted images, however, suggests that these sources are multiple (and possibly extended, at least in the case of source 5), which may indicate that their colors may have been altered by chance superposition with higher than average PSF subtraction artifacts. The real nature of these three detections cannot be determined with the current data, and a new observation to confirm

TABLE 3
Sources with Marginal or No Detection at 3.6 μm within 600 AU from ε Eri

Number	R.A.	Decl.	[3.6]	[4.5]	[3.6]−[4.5]	Distance (AU)
1..	53.189347	−9.444469	18.0 ± 0.6	17.29 ± 0.19	0.3 ± 0.6	512
2..	53.194310	−9.465338	19.2 ± 0.7	18.65 ± 0.07	0.5 ± 0.7	437
3..	53.194881	−9.465428	19.0 ± 0.7	18.52 ± 0.05	0.5 ± 0.7	430
4..	53.201029	−9.469290	19.7 ± 0.7	19.59 ± 0.15	0.1 ± 0.7	373
5[a].......................................	53.205047	−9.452265	>20.2	17.30 ± 0.17	>2.9	312
6[b].......................................	53.205817	−9.486791	>20.5	19.14 ± 0.10	>1.4	443
7..	53.206656	−9.489741	19.6 ± 0.6	19.32 ± 0.11	0.3 ± 0.6	464
8..	53.208558	−9.492060	19.7 ± 0.6	18.96 ± 0.06	0.7 ± 0.6	472
9..	53.213247	−9.454328	19.0 ± 0.6	18.66 ± 0.07	0.3 ± 0.6	214
10..	53.213330	−9.447145	19.5 ± 0.6	18.43 ± 0.07	1.1 ± 0.6	245
11..	53.213868	−9.414921	17.8 ± 0.5	17.70 ± 0.08	0.1 ± 0.5	543
12..	53.219017	−9.474964	19.2 ± 0.7	18.42 ± 0.07	0.8 ± 0.7	240
13..	53.219744	−9.481340	19.4 ± 0.8	17.57 ± 0.08	1.8 ± 0.8	299
14..	53.221378	−9.448212	18.7 ± 0.8	18.38 ± 0.11	0.3 ± 0.8	164
15..	53.223314	−9.488778	19.7 ± 0.6	18.50 ± 0.07	1.2 ± 0.6	366
16..	53.227599	−9.478849	19.0 ± 0.6	18.28 ± 0.05	0.3 ± 0.6	242
17..	53.229451	−9.440029	18.9 ± 0.6	17.85 ± 0.05	1.0 ± 0.6	213
18..	53.234574	−9.413988	18.6 ± 0.4	17.76 ± 0.07	0.8 ± 0.4	516
19..	53.236470	−9.497356	20.7 ± 1.9	19.13 ± 0.09	1.6 ± 1.9	458
20..	53.237040	−9.504618	19.3 ± 0.7	18.44 ± 0.06	0.9 ± 0.7	542
21..	53.238661	−9.440854	19.4 ± 0.9	18.46 ± 0.06	0.9 ± 0.9	220
22..	53.240732	−9.441868	19.1 ± 0.9	18.63 ± 0.09	0.5 ± 0.9	220
23..	53.249281	−9.498276	19.1 ± 0.9	18.60 ± 0.08	0.5 ± 0.9	509
24..	53.253290	−9.495511	17.7 ± 0.3	17.54 ± 0.03	0.2 ± 0.3	502
25..	53.258599	−9.484475	19.3 ± 0.7	18.48 ± 0.05	0.8 ± 0.7	440
26..	53.259360	−9.471248	19.1 ± 0.6	18.97 ± 0.09	0.1 ± 0.6	359
27..	53.268980	−9.431036	18.4 ± 0.4	17.70 ± 0.03	0.7 ± 0.4	541
28[c]......................................	53.269965	−9.487714	>20.2	17.64 ± 0.16	>2.6	565
29..	53.272692	−9.430506	18.7 ± 0.5	18.34 ± 0.07	0.4 ± 0.5	580

[a] Multiple or extended sources detected in all 4.5 μm images.
[b] Point source (possibly double) detected in second epoch 4.5 μm images.
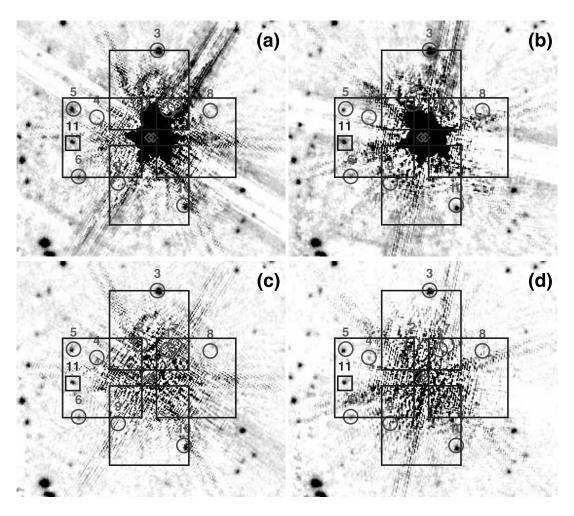[c] Point source (possibly multiple) detected in second epoch 4.5 μm images.

that they are real, and to measure their proper motion, is necessary to determine if they are physically associated to ε Eri.

4.4. Comparison with Keck AO and HST Searches

Even though none of our detected sources (with the possible exception of the three 3.6 μm "dropout sources" described in § 4.3) have the colors or magnitudes to be low-mass companions of ε Eri, it is still useful to compare the results of our survey with the previous M03 search. Figure 10 shows the location, in our 4.5 μm images, of the 10 objects identified by M03 in their K-band Keck AO maps within an area roughly ≈40″ (≈130 AU) from ε Eri. We detected four of these objects (numbered 3, 5, 6, and 10) in at least two IRAC images. We could not detect sources 1, 2, 4, 7, 8, and 9, which are below the PSF-subtraction residual noise in their position. We have, however, detected one source that was missed in the Keck search (inside box number 11). A careful examination of the Keck plates (M03, Fig. 2) indeed shows the presence of a faint source (below the Keck observations detection limit) in the location of source 11. Sources 4, 6, and 11 have also been detected by P04; they have an extended source appearance and are probably background galaxies.

Table 4 summarizes the properties of the M03 sources. The "Keck Coordinates" columns indicate the position of each source at the time of the M03 first epoch (2001 December). Since Table 3 in M03 does not provide absolute coordinates for the sources but only offsets from ε Eri, we had to derive their actual R.A. and decl. by estimating the position of ε Eri in 2001 De-

cember from the ICRS 2000 (Perryman et al. 1997) coordinates and proper motion. Given that M03 had to keep ε Eri outside their field of view to limit PSF artifacts, the accuracy of the 2001 December coordinates is limited to 0″.2, which is the precision with which M03 can establish the position of ε Eri relative to their images. We then estimated the coordinates of each source at the time of the first IRAC epoch (2004 January) by extrapolating the motion measured by M03 between 2001 December and their second epoch in 2002 August. Note that the predicted 2004 position cannot be derived for some of the sources, either because they were used as position reference or because the second epoch was missing (source 3). Given the high accuracy quoted by M03 in the relative shift measurements, the uncertainty of the predicted coordinates in the IRAC images is still dominated by the uncertainty in their 2001 absolute coordinate of 0″.2.

Finally, we determined the position of all sources detected within the Keck field of view by measuring their photocenter in the IRAC 4.5 μm images. The uncertainty in the measurement of the sources' centroid is limited by the presence of PSF subtraction artifacts and second epoch source aliasing, but is consistent, between our two epochs, with an accuracy of 0″.2. Within this limit, we did not observe any shift in the source coordinates between the two IRAC epochs. The real uncertainty in the IRAC coordinates, however, is much larger than 0″.2, due to systematic errors in the pointing of the spacecraft. These errors are normally corrected by a pointing refinement procedure, included in the Spitzer Space Center data reduction pipeline, which uses 2MASS

Fɪɢ. 10.—IRAC 4.5 μm images of the area surrounding ε Eri that was searched by M03: (*a*) Epoch 1 PSF subtracted, (*b*) epoch 2 PSF subtracted, (*c*) epoch 1–epoch 2, and (*d*) epoch 2–epoch 1. The large squares are the field of view of the individual Keck images (40″ size). The circles marks the positions of the sources found in the M03 search extrapolated to their expected position at the epoch of the IRAC observations. The small box indicates a source found in our IRAC images that was missed in M03. The two little diamonds indicate the position of ε Eri at the time of the first Keck epoch (*left diamond*), and the IRAC (*right diamond*) observations. [*See the electronic edition of the Journal for a color version of this figure.*]

stars (Cutri et al. 2003) to find an absolute reference frame for the IRAC images within the 0″.15 2MASS accuracy. In the case of ε Eri, however, this pointing refinement was not done because no 2MASS sources are detected in the vicinity (because of the ε Eri glare saturating the 2MASS detectors). The headers of the IRAC BCD frames show a pointing accuracy error of ∼1″ at the time of our observations.

By comparing the coordinates of all sources detected in both the Keck and IRAC images, we have measured the shift between 2001 December and 2004 January. The values we obtained, listed in Table 4, are rather large and appear to suffer a systematic shift, possibly due to the limitations in the *Spitzer* pointing accuracy described above. We have tried to correct this systematic shift by subtracting the average value of the measured shift of 0″.13 in R.A. and 1″.30 in decl. We estimate the uncertainty of the final shifts to be of the order of ∼1″. A significant fraction of this uncertainty may be due to the different centroid that partially resolved extragalactic sources, if extended or multiple, may have in the *K* and 4.5 μm bands. Within this error, none of the sources show a measurable proper motion, and the corrected shifts listed in Table 4 are all well below the expected ε Eri proper motion between the Keck and IRAC observations of more than 2″ in R.A. We also did not find any significant shift between the co-ordinates of sources 4, 6, and 11, as measured in the IRAC 4.5 μm

images and the *HST* STIS P04 maps. This confirms that none of the sources detected in the common field of view with the Keck and P04 observations is a low-mass companion of ε Eri.

5. CONCLUSIONS

As the number of exoplanets detected with radial velocity or eclipsing techniques since the initial detection by Mayor & Queloz (1995) continue to grow, the payoff of directly detecting their thermal emissions cannot be underestimated. As of today, thermal radiation has been directly detected from only three planets, all of them eclipsing "hot Jupiters" whose light has been detected with *Spitzer*: TrES-1 with IRAC (Charbonneau et al. 2005) at 4.5 and 8.0 μm, HD 209458b (Deming et al. 2005) with MIPS 24 μm, and HD 189733b with IRS (Deming et al. 2006). These three detections allowed for the first time a comparison between theoretical models of hot Jupiters with real data. How-ever, no direct detection of gas giants orbiting a nearby parent star at a distance comparable to our own Jupiter and Saturn has been achieved so far, as all searches conducted from the ground (M03) and from space (P04 and this one) have returned negative results. Models of giant planets orbiting systems analogous to the solar system are thus still untested.

While future space missions, such as the *James Webb Space Telescope* and the *Terrestrial Planet Finder*, are being designed

TABLE 4
Proper Motion and Photometry of M03 Objects

Number	Keck Coordinates[a]		IRAC Coordinates		Predicted[b]		Measured[b,c]		Corrected[b,c,d]		Photometry[e]				
	R.A.	Decl.	R.A.	Decl.	$\Delta\alpha$	$\Delta\delta$	$\Delta\alpha$	$\Delta\delta$	$\Delta\alpha$	$\Delta\delta$	[K]	[3.6]	[4.5]	[5.8]	[8.0]
ϵ Eri........	53.23216	−9.45825	53.23159	−9.45824	2.05	−0.04									
1..............	53.22949	−9.45431	...	...	...	...	...	...	...	...	17.3	...	...	...	...
2..............	53.23341	−9.45353	...	...	...	...	...	...	...	...	17.3	...	...	...	...
3..............	53.23099	−9.44600	53.23085	−9.44634	...	...	0.50	1.22	0.37	−0.08	16.3	15.4	15.4	15.5	15.4
4[f]............	53.23960	−9.45539	...	...	−0.03	0.01	...	...	...	...	19.4	...	...	...	...
5..............	53.24291	−9.45422	53.24316	−9.45455	0.05	0.28	−0.90	1.19	−1.03	−0.11	20.7	17.4	16.5	15.1	15.7
6[f]............	53.24219	−9.46369	53.24212	−9.46390	0.09	−0.03	0.25	0.76	0.12	−0.54	20.2	17.6	17.1	...	...
7..............	53.22852	−9.45369	...	...	0.05	0.16	...	...	...	...	20.3	...	...	...	...
8..............	53.22343	−9.45447	...	...	0.08	0.00	...	...	...	...	20.1	...	...	...	...
9..............	53.23658	−9.46461	...	...	−0.10	0.06	...	...	...	...	20.8	...	...	...	...
10............	53.22722	−9.46772	53.22703	−9.46828	0.06	0.10	0.68	2.01	0.55	0.71	19.3	16.7	16.2	...	15.7
11[f]	...	...	53.24301	−9.45902	...	...	...	...	...	...	...	...	16.5	...	15.3

[a] Positions calculated for Keck first epoch, 2001 December 1.
[b] Shifts expressed in seconds of arc.
[c] Shift statistical uncertainty is 0″.2.
[d] Shifts corrected by subtracting the average shift of 0″.13 in R.A. and 1″.30 in decl.
[e] Average statistical error in IRAC photometry is 0.2 mag.
[f] Detected in P04 as extended structures.

with the goal of direct exoplanetary detection, this work shows that the *Spitzer Space Telescope* with the IRAC camera already has the capability of detecting young gas giants with a mass as low as a few M_J if they are orbiting their parent star at a distance comparable to our own solar system Kuiper belt. Planets ejected on very elongated orbits during the initial phases of planetary system formation can be detected with *Spitzer*/IRAC down to masses of $1M_J$. Our observations allow to set a limit of $\sim 2M_J$ at the distance of ~ 60 AU ($\sim 18''$) from the star, and $\lesssim 1M_J$ outside the debris disk ring ($\sim 35'' \simeq 112$ AU).

Comparison with M03 confirms that within our search space we are able to detect all the sources found with the most sensitive ground-based search outside a radius of ~ 130 AU and, in addition, one below the Keck sensitivity. Comparison with the position of the common sources between IRAC and Keck observations confirms that none of the detections match the proper motion required to be a physical companion of ϵ Eri, validating and extending the M03 results.

On the basis of the colors of the detected sources, we did not find any strong companion candidate. However, for a number of sources listed in Table 3, we are missing a detection in the 3.6 μm IRAC band. Without a good [3.6]−[4.5] color we cannot determine the nature of these sources, and a second epoch is necessary to measure their proper motion. Given the positional accuracy in the PSF-subtracted IRAC frames of $\sim 1''$, such a measurement will be feasible after a time lag of about 2 years from the current observations.

REFERENCES

Backman, D. E., & Paresce, F. 1993, in Protostar and Planets III, ed. E. H. Levy & J. I. Lunine (Tucson: Univ. Arizona Press), 1253
Barmby, P., et al. 2004, ApJS, 154, 97
Becklin, E., & Zuckerman, B. 1988, Nature, 336, 656
Beichman, C. A. 1987, ARA&A, 25, 521
Benedict, G. F., & McArthur, B. E. 2004, AAS DPS Meeting 36, 42.02
Burrows, A., Sudarsky, D., & Lunine, J. I. 2003, ApJ, 596, 587
Burrows, A., et al. 1997, ApJ, 491, 856
Chabrier, G., & Baraffe, I. 1997, A&A, 327, 1039
Charbonneau, D., et al. 2005, ApJ, 626, 523
Cohen, M., Megeath, S. T., Hammersley, P. L., Martín-Luis, F., & Stauffer, J. 2003, AJ, 125, 2645
Cutri, R. M., et al. 2003, 2MASS All-Sky Catalog of Point Sources (Caltech: IPAC), http://irsa.ipac.caltech.edu/applications/Gator
Deming, D., Harrington, J., Seager, S., & Richardson, L. J. 2006, ApJ, 644, 560
Deming, D., Seager, S., Richardson, L. J., & Harrington, J. 2005, Nature, 434, 740
Di Folco, E., Thévenin, F., Kervella, P., Dominiciano de Souza, A., Coudé du Foresto, V., Ségransan, D., & Morel, P. 2004, A&A, 426, 601
Donahue, R. A., Saar, S. H., & Baliunas, S. L. 1996, ApJ, 466, 384
Fazio, G. G., et al. 2004a, ApJS, 154, 10
———. 2004b, ApJS, 154, 39
Fix, E., & Hodges, J. L. 1951, USAF School Aviation Medical Rep. 4
Ford, E. B., Havlickova, M., & Rasio, F. A. 2001, Icarus, 150, 303
Gillett, F. C. 1986, in Light on Dark Matter, Proc. First Infra-Red Astronomical Satellite Conf. (Dordrecht: Reidel), 61
Greaves, J. S., et al. 1998, ApJ, 506, L133
———. 2005, ApJ, 619, L187
Gutermuth, R. A., Megeath, Muzerolle, J., Allen, L. E., Pipher, J. L.; Myers, P. C., & Fazio, G. G. 2004, ApJS, 154, 374
Hatzes, A. P., et al. 2000, ApJ, 544, L145
Houck, J. R., et al. 2004, ApJS, 154, 18
Huang, J.-S., et al. 2004, ApJS, 154, 44
Li, A., Lunine, J. I., & Bendo, H. J. 2003, ApJ, 598, L51

Macintosh, B. A., Beicklin, E. E., Kaisler, D., Konopacky, Q., & Zuckerman, B. 2003, ApJ, 594, 538 (M03)
Mathis, J. S., Rumpl, W., & Nordsieck, K. H. 1977, ApJ, 217, 425
Mayor, M., & Queloz, D. 1995, Nature, 378, 355
Moran, S. M., Kuchner, M. J., & Holman, M. J. 2004, ApJ, 612, 1163
Nakajima, T., Oppenheimer, B. R., Kulkarni, S. R., Golimowski, D. A., Matthews, K., & Durrance, S. T. 1995, Nature, 378, 463
Ozernoy, L. M., Gorkavyi, N. N., Mather, J. C., & Taidakova, T. A. 2000, ApJ, 537, L147
Patten, B. M., et al. 2004, AAS Meeting 205, 17.09
———. 2006, ApJ, in press

Perryman, M. A. C., et al. 1997, A&A, 323, 49
Proffitt, C. R., et al. 2004, ApJ, 612, 481 (P04)
Quillen, A. C., & Thorndike, S. 2002, ApJ, 578, L149
Rieke, G. H., et al. 2004, ApJS, 154, 25
Saar, S. H., & Osten, R. A. 1997, MNRAS, 284, 803
Sheret, I., Dent, W. R. F., & Wyatt, M. C. 2004, MNRAS, 348, 1282
Spitzer Science Center. 2004, Infrared Array Camera Data Handbook (Pasadena: SSC), http://ssc.spitzer.caltech.edu/irac/dh
Stapelfeldt, K. R., et al. 2004, ApJS, 154, 458
Su, K. Y. L., et al. 2005, ApJ, 628, 487
Werner, M. W., et al. 2004, ApJS, 154, 1